Kinetics and thermochemistry of the reaction of 3-methylpropargyl radical with molecular oxygen

Pekkanen, Timo T.

2019

Pekkanen , T T , Timonen , R S , Lendvay , G , Rissanen , M P & Eskola , A J 2019 , ' Kinetics and thermochemistry of the reaction of 3-methylpropargyl radical with molecular oxygen ' , Proceedings of the Combustion Institute , vol. 37 , no. 1 , pp. 299-306 . https://doi.org/10.1016/j.proci.2018

http://hdl.handle.net/10138/325133
https://doi.org/10.1016/j.proci.2018.05.050

Kinetics and Thermochemistry of the Reaction of 3-Methylpropargyl Radical with Molecular Oxygen

Timo T. Pekkanen[a], Raimo S. Timonen[a], György Lendvay[b], Matti P. Rissanen[c], Arkke J. Eskola[a,*]

[a]*Department of Chemistry, University of Helsinki, P.O. Box 55 (A.I. Virtasen aukio 1), 00014 Helsinki, Finland*
[b]*Institute of Materials and Environmental Chemistry, Research Centre for Natural Sciences, Hungarian Academy of Sciences, Magyar Tudsok krt. 2., Budapest H-1117, Hungary*
[c]*Department of Physics, University of Helsinki, P.O. Box 64 (A.I. Virtasen aukio 1), 00014 Helsinki, Finland*

Abstract

We have measured the kinetics and thermochemistry of the reaction of 3-methylpropargyl radical (but-2-yn-1-yl) with molecular oxygen over temperature (223 − 681 K) and bath gas density ($1.2 - 15.0 \times 10^{16}$ cm^{-3}) ranges employing photoionization mass-spectrometry. At low temperatures (223 − 304 K), the reaction proceeds overwhelmingly by a simple addition reaction to the $-CH_2$ end of the radical, and the measured $CH_3CCCH_2^{\bullet} + O_2$ reaction rate coefficient shows negative temperature dependence and depends on bath gas density. At intermediate temperatures (340−395 K), the addition reaction equilibrates and the equilibrium constant was determined at different temperatures. At high temperatures (465 − 681 K), the kinetics is governed by O_2 addition to the third carbon atom of the radical, and rate coefficient measurements were again possible. The high temperature $CH_3CCCH_2^{\bullet} + O_2$ rate coefficient is much smaller than at low T, shows positive temperature dependence, and is independent of bath gas density. In the intermediate and high temperature ranges, we observe a formation signal for ketene (ethenone). The reaction was further investigated by combining the experimental results with quantum chemical calculations and master equation modeling. By making small adjustments (2 − 3 kJ mol^{-1}) to the energies of two key transition states, the model reproduces the experimental results within uncertainties. The experimentally constrained master equation model was used to simulate the $CH_3CCCH_2^{\bullet} + O_2$ reaction system at temperatures and pressures relevant to combustion.

Keywords:
Experimental Gas Kinetics, Master Equation Modeling, Ab Initio Quantum Chemistry, Combustion Chemistry, Propargyl Radical

*Corresponding author:
Email address: arkke.eskola@helsinki.fi (Arkke J. Eskola)

1. Introduction

Resonance-stabilized hydrocarbon radicals (RSHRs) show decreased reactivity towards O_2 when compared to similar sized radicals without resonance-stabilization.[1] Because of this, RSHRs can reach high enough concentrations under combustion environments for their self-reactions to become important.[2] These self-reactions can lead to the formation of aromatic rings, which is the first step in soot formation.[3] Soot is an unwanted by-product of practical combustion, e.g. in internal combustion engines, and in order to minimize soot formation, the underlying mechanism needs to be understood. In combustion environments, the key reactions[2] that produce the first aromatic rings and initiate soot formation are the following:

$$HCCCH_2^\bullet + HCCCH_2^\bullet \longrightarrow C_6H_6 \text{ (benzene)} \quad (1)$$

$$CH_3CCCH_2^\bullet + HCCCH_2^\bullet \longrightarrow C_7H_8 \text{ (toluene)} \quad (2)$$

$$CH_3CCCH_2^\bullet + CH_3CCCH_2^\bullet \longrightarrow C_8H_{10} \text{ (xylene)} . \quad (3)$$

The reactions of $HCCCH_2^\bullet$ (propargyl) and $CH_3CCCH_2^\bullet$ (3-methylpropargyl) radicals with O_2 compete with the aromatic ring formation reactions (1) − (3). In order to understand conditions where reactions (1) − (3) become important, it is essential to understand the kinetics of $HCCCH_2^\bullet + O_2$ and $CH_3CCCH_2^\bullet + O_2$ reactions. The

$$HCCCH_2^\bullet + O_2 \longrightarrow \text{ Products} \quad (4)$$

reaction has received attention previously,[4–7] but to our knowledge, the reaction under study in this work,

$$CH_3CCCH_2^\bullet + O_2 \xrightarrow{k_5} \text{ Products} , \quad (5)$$

has not been investigated before.

A general feature of RSHR + O_2 addition reactions is that the reverse dissociation reaction back to reactants becomes important at much lower temperatures than for ordinary hydrocarbon + O_2 reactions.[4, 6, 8, 9] Consequently, the RSHR + O_2 reaction will be a "dead-end" in combustion environments unless new reaction pathways become available at higher temperatures. A bimolecular product channel has been observed for reaction (4) at 500 K, whereas for the allyl radical + O_2 reaction, any bimolecular product channel is extremely slow (4.15×10^{-19} cm^3 s^{-1}) even at as high as 753 K.[4, 10]

In the present work, we have studied the kinetics and thermochemistry of reaction (5) as a function of temperature and bath gas density. The reaction was studied both experimentally and computationally. The computational work consists of DFT calculations, high-level ab initio calculations, and master equation modeling. Although we did not perform the experiments under combustion-relevant conditions, our experimental results are vital in constraining key parameters in our master equation model. The model could then be used to simulate the kinetics of reaction (5) up to combustion-relevant conditions with high temperature and pressure.

2. Experimental

Experiments were performed in a laminar flow reactor coupled to a photoionization mass-spectrometer and excimer laser photolysis of the CH_3CCCH_2Br precursor at 193 or 248 nm wavelength was used for radical production. The experimental apparatus and data analysis for kinetic measurements have been described in a previous publication.[11] The experimental details relevant to this work are given in the Supplemental Material.

3. Quantum Chemistry

The geometries of the stationary points on the potential energy surface (PES) of reaction (5) were optimized at the MN15/Def2TZVP level of theory.[12, 13] Intrinsic reaction coordinate calculations were performed to verify that each saddle point connected the right local minima. The same level was also used to compute harmonic frequencies, zero-point energies (ZPE) and numeric one-dimensional hindered rotor potentials (5° increments). The computed harmonic frequencies were scaled by a factor of 0.993 and zero-point energies by a factor of 0.979.[14] The hindered rotor potentials were computed with relaxed PES scans. All quantum chemistry calculations were done with the Gaussian 16 software.[15]

Based on the MN15/Def2TZVP results, the energetics of the key structures were calculated at ROHF-CCSD(T)/cc-pVDZ, ROHF-CCSD(T)/cc-pVTZ and ROHF-CCSD(T)/cc-pVQZ levels of theory.[16] The relation

$$\Delta E_{\text{CBS}} = \Delta E_{\text{cc-pVQZ}} - (\Delta E_{\text{cc-pVTZ}} - \Delta E_{\text{cc-pVQZ}}) \frac{4^4}{5^4 - 4^4} \quad (6)$$

was used to obtain electronic energies at the complete basis set (CBS) limit.[17,18] Here ΔE is the energy relative to the reactant energy. For test purposes, we also extrapolated CBS energies from cc-pVDZ and cc-pVTZ calculations and found that the energies usually differed only by a few kJ mol^{-1} compared to the cc-pVTZ and cc-pVQZ extrapolated energies (see Table S1).

4. Master Equation Modeling

Master equation modeling was carried out using the MESMER software (version 5.1).[17] MESMER uses RRKM theory to calculate microcanonical rate coefficients for reactions with well defined transition states. It is a one-dimensional master equation code, which means that only the rovibrational energy of the system is treated as an independent variable, while angular momentum effects are considered only in an average manner. Failing to account for angular momentum effects causes some uncertainty, but it is not believed to be the dominant source of uncertainty for most reactions.[17] For barrierless addition reactions, MESMER uses the Inverse Laplace Transform (ILT) approach to calculate microcanonical rate coefficients. The expression MESMER transforms is the modified Arrhenius equation

$$k_\infty(T) = A\left(\frac{T}{T_0}\right)^m \mathrm{e}^{-\frac{E_a}{RT}} , \tag{7}$$

where $k_\infty(T)$ is the rate coefficient at the high pressure limit, A is the pre-exponential factor, T is the temperature, T_0 is some reference temperature, m is the modified Arrhenius parameter, and E_a is the activation energy. T_0 is typically chosen as 300 K (or 298 K). For barrierless reactions, E_a is small and can be set to zero; any T-dependence is carried by m. If experimental data is provided, it is possible to use MESMER's built-in non-linear least squares fitting algorithm (Levenberg-Marquardt algorithm) to obtain the Arrhenius parameters that best reproduce experimental data.

MESMER uses the equation

$$\langle\Delta E\rangle_{\mathrm{down}} = \langle\Delta E\rangle_{\mathrm{down,ref}}\left(\frac{T}{T_{\mathrm{ref}}}\right)^n \tag{8}$$

to model the collisional energy transfer for reaction intermediates (local minima on a PES). Here $\langle\Delta E\rangle_{\mathrm{down,ref}}$ is an energy transfer parameter at some reference temperature (typically 300 K) and n is a parameter that governs the temperature dependence of the energy transfer parameter. $\langle\Delta E\rangle_{\mathrm{down,ref}}$ and n can be fitted to experimental data the same way as the Arrhenius parameters. A Lennard-Jones (LJ) collision model is used to calculate the collision frequency. This model requires the user to provide two additional input parameters, the depth of the potential well ϵ_{LJ} and the finite length where the potential is zero σ_{LJ}.

5. Results and Discussion

5.1. Experimental

At low temperatures (220 – 304 K), the measured bimolecular rate coefficient k_5 for 3-methylpropargyl disappearance exhibits negative temperature dependence and also depends on bath gas density. At intermediate temperatures (336 – 395 K), the radical signals do not show single-exponential decay and return to the pre-photolysis baseline very slowly, indicating that a dissociation reaction back to reactants is taking place. In this temperature range, a double-exponential fitting function[9] was used to obtain the rate coefficient for both the forward and reverse reaction, which were then used to determine the equilibrium constant (assuming gases are ideal and their standard states chosen as pure gas at 1 bar at the temperature of interest). At high temperatures ($T \geq 465$ K), the signal again decays back to the pre-photolysis baseline, enabling rate coefficient measurements. In this temperature range, the measured bimolecular rate coefficient k_5 exhibits positive temperature dependence and is independent of bath gas density. Plots of the experimental results are given in Fig. 1 and Fig. 2. Tables listing the experimental results and conditions for each measurement are given in the Supplemental Material (Tables S2, S3, and S4). We estimate the overall uncertainty of the bimolecular rate coefficient and equilibrium constant measurements to be ±20% and ±15%, respectively. The uncertainties arise mainly from uncertainties in signal fitting and in O_2 concentrations, the latter resulting from the uncertainties in measured flow rates.

When seeking for reaction products, we observed a reaction product at $m/z = 42$ in the intermediate and high temperature ranges. This corresponds almost certainly to ketene (ethenone). If ketene is formed, one would assume that acetyl radical is also formed. However, we were not able to observe the formation of acetyl radical. This leads us to believe that acetyl radical either instantly dissociates or reacts with O_2 after its formation. Methyl radical is the dissociation product of acetyl along with carbon monoxide, but because the $CH_3^\bullet + O_2$ rate coefficient is about an order of magnitude larger than the $CH_3CCCH_2^\bullet + O_2$ rate coefficient at high temperatures,[18] any methyl radicals that are formed will instantly react with oxygen, making detection difficult. A detailed list of products sought is reported in the Supplemental Material.

Overall, reaction (5) appears to behave very similar to reaction (4) measured by Slagle and Gutman.[4] They also observed bath gas density dependence and negative temperature dependence at low temperatures ($T \leq 333$ K), equilibrium behavior at intermediate temperatures (380−430 K), and positive temperature dependence and independence from bath gas density at high temperatures ($T \geq 500$ K). Similarly, they observed ketene as a reaction product at equilibrium temperatures

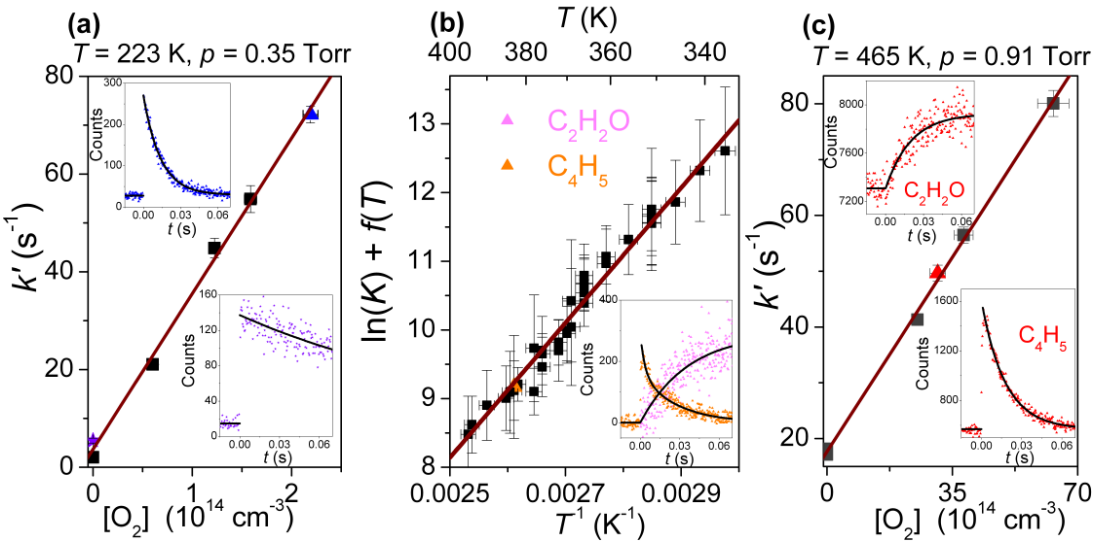

Figure 1: **(a):** A typical bimolecular plot at low temperature. A radical decay signal in the absence of O_2 is shown in the bottom right corner. A radical decay signal with added oxygen is shown in the top left corner. **(b):** A modified van't Hoff plot of $\ln(K) + f(T)$ versus reciprocal temperature. See text for details.**(c):** A typical bimolecular plot at high temperature. A radical decay signal with added oxygen is shown in the bottom right corner. The corresponding formation signal for ketene is shown in the top left corner. The radical decay rate is 49.6 ± 1.5 s^{-1} and the ketene formation rate is 50.3 ± 4.1 s^{-1}. The uncertainties are the standard errors (1σ) of the fits.

and above. All of this suggests that the reaction mechanism for reaction (5) is the same as for reaction (4), at least under the experimental conditions covered in this work. The main differences between the two reactions are that equilibrium behavior is observed for reaction (5) roughly 50 K earlier than for reaction (4) and that the bimolecular rate coefficient of reaction (5) is about an order of magnitude larger in the low temperature falloff region. However, in the high temperature regime k_5 is only about 2 or 3 times larger.

5.2. *Quantum Chemistry*

A detailed reaction enthalpy profile at zero kelvin for the PES of reaction (5) is presented in the Supplemental Material along with a comprehensive table listing all the relevant energies for each stationary point (Fig. S1 and Table S1), and the relevant optimized geometries can also be found in the Supplemental Material (geometries.txt). Figure 3 presents a reaction enthalpy profile at zero kelvin corresponding to the part of the PES of reaction (5) that was included in our master equation model. The profile is obtained by omitting elementary steps that do not significantly affect the overall kinetics of reaction (5). The final reaction in Fig. 3, TS2a → P, represents an infinite sink in the master equation model. The electronic and zero-point energies of each species in Fig. 3 are listed in Table 1. Some harmonic frequencies were replaced with one-dimensional hindered rotors and the zero-point energies were corrected accordingly.

The electronic structure of highly unsaturated open-shell systems, especially those away from geometries of stable species, is generally not easy to calculate precisely. Unrestricted open-shell methods generate large, often unacceptable spin contamination, depreciating the reliability of the calculated energies. In addition, such systems involve significant non-dynamical correlation, requiring multireference treatment. A way to estimate the importance of the multireference character is the T1 diagnostic:[19] when it is above 0.04, one can expect significant multireference effects. As can be seen in Table 1, this index is large for transition structures TS1a and TS2a. Furthermore, at the MN15/Def2TZVP geometry of TS2a we identified three close-lying electronic states (see Table S1), which also indicates the single-configuration methods are probably not reliable for such structures. Considering that the rather detailed and careful efforts presented in Ref. 7 proved inconclusive concerning the proper method to estimate the height of the analog of TS1p for reaction (4), we chose not to explore the multireference character of TS1a and TS2a further. Instead, our most accurate energies were calculated with a high-level treatment of electron correlation based on the restricted open-shell Hartree-Fock reference, ROHF-CCSD(T), which does not suffer from spin contamination errors. ROHF-CCSD(T) also includes,

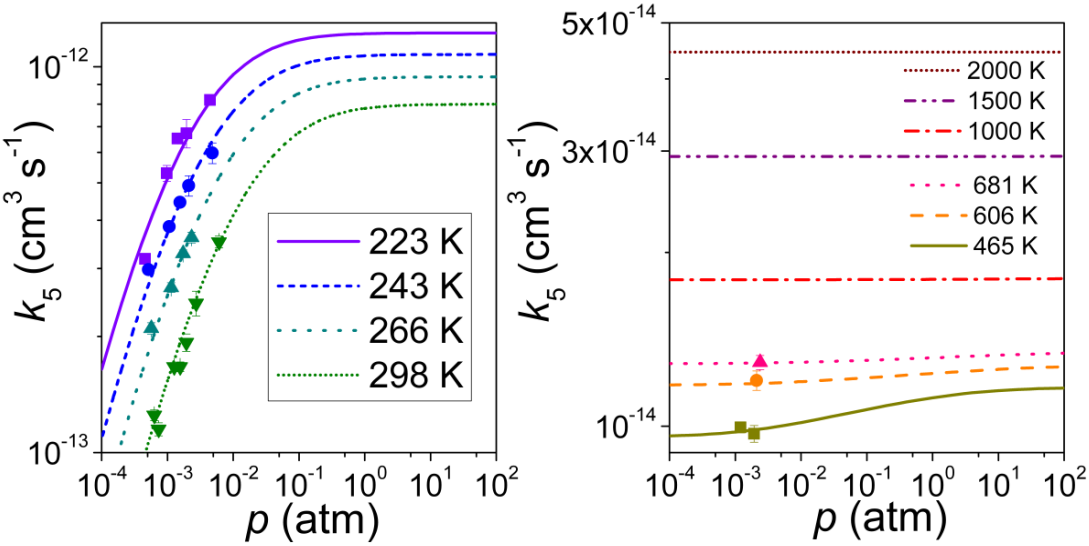

Figure 2: The symbols in the left and right subfigures depict the $CH_3CCCH_2^{\bullet} + O_2$ bimolecular rate coefficient measured at different temperatures and pressures. The experimental results (symbols) are shown alongside the results produced by our master equation model (lines).

especially at the (T) level, many of the important configurations. With this method, we performed basis set extrapolation, keeping in mind that the computed energies of TS1a and TS2a remain more uncertain than those of the other species. For the species where multireference effects are not significant, we believe that our computational method should reach chemical accuracy (roughly ± 4 kJ mol^{-1}). This is supported by the very good agreement between the CBS limit of the ROHF-CCSD(T) energies and those obtained with the G4 method (see Table S1). The ROHF-CCSD(T) calculations were performed at the MN15/Def2TZVP geometries, except TS1a, for which the M06-2X/Def2TZVP[20] structure was used (because with the MN15 functional no saddle point was detected).

Our reaction enthalpy profile is very similar to that obtained by Hahn and co-workers in their study of reaction (4).[6] The main difference is that we found the pathway via the four-membered ring, TS2a, to be lower in energy than that via the three-membered ring (TS4a, see Fig. S1, Fig. S2, and Table S1). Note that Hahn and co-workers report that many of their key transition structures suffer from massive spin contamination and that one should be careful in interpreting their energies.

At the MN15/Def2TZVP level of theory, a well-defined saddle point was found for the initial R $\rightarrow$ Int1p addition reaction (TS1p). The ROHF-CCSD(T) single-point calculations brought the energy of this transition state just below the reactant energy (see Table S1). However, the energy is probably not very reliable, since the transition state structure has a T1 diagnostic value of 0.052, which indicates a strong multireference character that our method can not account for. In our master equation model, we assumed the R $\rightarrow$ Int1p reaction to be barrierless. We feel confident that this reaction is really barrierless because our conclusion is consistent with our experimental findings. Furthermore, an extensive multireference study done on the corresponding reaction for propargyl radical found the addition reaction to be barrierless,[7] but it left open the possibility that a submerged barrier might exist. Should it exist, it is predicted to be $5 - 10$ kJ mol^{-1} below the reactant energy.

5.3. Master Equation Modeling

The input file of our master equation model is given in the Supplemental Material (mesmerInputFile.xml). MESMER's ILT approach was used to obtain microcanonical rate coefficients for the barrierless R $\rightarrow$ Int1p reaction. We used the following Arrhenius parameters:

$$A = 7.71 \times 10^{-13}\ \text{cm}^3\ \text{s}^{-1} \qquad T_0 = 300\ \text{K}$$
$$m = -1.49 \qquad E_a = 0\ .$$

A and m were determined according to a least squares fit to the experimental data. The collisional energy transfer and collisional frequency parameters used for Int1p and Int1a were

$$\langle \Delta E \rangle_{\text{down,ref}} = 172\ \text{cm}^{-1} \qquad \epsilon_{\text{LJ}} = 465\ \text{K}$$
$$T_{\text{ref}} = 300\ \text{K} \qquad \sigma_{\text{LJ}} = 6.3\ \text{Å}$$
$$n = 0.43\ .$$

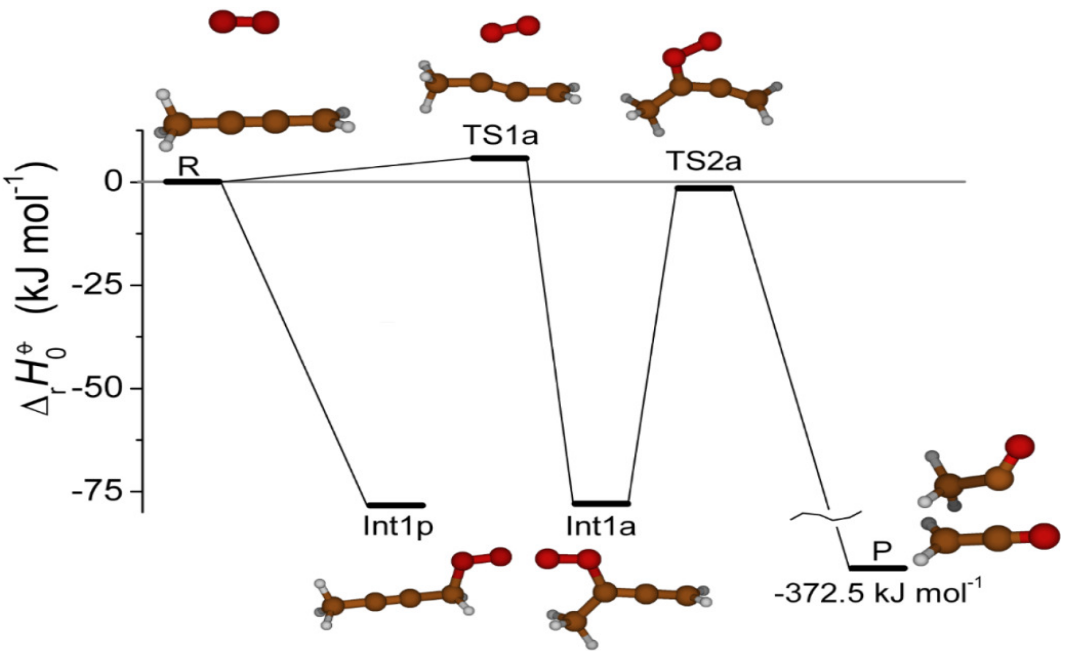

Figure 3: A reaction enthalpy profile at zero kelvin corresponding to the part of the PES of reaction $CH_3CCCH_2^\bullet + O_2$ that is included in our master equation model. Elementary steps that do not significantly affect the overall kinetics of $CH_3CCCH_2^\bullet + O_2$ have been omitted.

The parameters $\langle \Delta E \rangle_{\text{down,ref}}$ and n were simultaneously fitted with A and m. The optimum value for $\langle \Delta E \rangle_{\text{down,ref}}$ is close to the 200 cm^{-1} value used in other works involving similar sized molecules, while the value obtained for n is a bit lower than the typically used n = 0.85.[21–24] The LJ parameters ϵ_{LJ} and σ_{LJ} are not available for Int1p or Int1a, so we used the online resources of Cantherm[25] to look up LJ parameters for similar molecules. These values were then used to estimate the LJ parameters of Int1p and Int1a.

To reproduce the experimental data at high temperatures ($T \geq 465$ K), the barrier heights corresponding to TS1a and TS2a had to be lowered by 2.0 and 3.0 kJ mol^{-1}, respectively. TS2a is the kinetic bottleneck at high temperatures, so we first used the rate coefficient measured at 681 K for an initial adjustment of TS2a. Then we used the rate coefficient data at 465 K, where both TS1a and TS2a are kinetically relevant, to adjust TS1a along with minor adjustments to TS2a. These slight adjustments are well within the accuracy of our computational method. With these adjustments, our master equation simulations are in excellent agreement with the experimental results (see Fig. 2 and Table S2). Without these adjustments, the high temperature rate coefficient returned by our master equation calculations was roughly 50% of the experimental value.

In Fig. S3 we show the temperature dependence of some of the elementary reaction rate coefficients returned by our master equation calculations at pressures 0.0001 atm and 100 atm. Here it is interesting that the products can be formed by either a well-skipping reaction

$$\mathrm{R} \xrightarrow{k_{\text{ws}}} \mathrm{P}$$

or through the channel

$$\mathrm{R} \underset{k_{\text{b}}}{\overset{k_{\text{f}}}{\rightleftharpoons}} \mathrm{Int1a} \xrightarrow{k_{\text{p}}} \mathrm{P}$$

. The former dominates at low pressures and the latter at high pressures. At temperatures beyond 1500 K, the products are formed exclusively through the well-skipping reaction channel. Below 1500 K and at intermediate pressures, both channels account for R loss and the effective loss rate is approximately

$$k_{5,\text{eff}} = k_{\text{ws}} + k_{\text{f}} \left(1 - \frac{k_{\text{b}}}{k_{\text{b}} + k_{\text{p}}} \right) ,$$

where the term

$$k_{\text{f}} \left(1 - \frac{k_{\text{b}}}{k_{\text{b}} + k_{\text{p}}} \right)$$

is obtained by using the steady-state approximation for Int1a. We tested the validity of the steady-state approximation by comparing $k_{5,\text{eff}}$ to the loss rate obtained by doing a simple one-exponential decay fit to

Table 1: Energies of the stationary points on the $CH_3CCCH_2^{\bullet} + O_2$ PES that are included in our master equation model. All energies are relative to the reactant energy. The table lists the T1 diagnostic, the electronic energy at the complete basis set limit (see Equation (6)), the zero-point energy and the zero-point corrected electronic energy (standard enthalpy of reaction at zero kelvin). The final column shows the experimentally adjusted $\Delta_r H_0^{\ominus}$ used in our master equation model.

Species	Structure	T1	ΔE_{CBS} (kJ mol^{-1})	ΔZPE (kJ mol^{-1})	$\Delta_r H_0^{\ominus}$ (kJ mol^{-1})	Adj. (kJ mol^{-1})
R	$CH_3CCCH_2^{\bullet} + O_2$	0.026, 0.017	0	0	0	
Int1p	$CH_3CCCH_2OO^{\bullet}$	0.024	−97.36	18.92	−78.43	
Int1a	$CH_3C(OO^{\bullet})CCH_2$	0.032	−95.02	16.92	−78.10	
P	$CH_2CO + CH_3C^{\bullet}O$	0.017, 0.023	−375.4	2.928	−372.5	
TS1a[a]	R → Int1a	0.044	0.4018	7.277	7.679	5.700
TS2a[b]	Int1a → P	0.038	−10.96	12.42	1.460	−1.500

[a] Geometry optimized at the M06-2X/Def2TZVP level of theory.
[b] For TS2a, data for the lowest electronic state is presented. See text and Table S1 for details.

the species/time profile of R as calculated by MESMER. At 450 K, the rate coefficient yielded by the steady state approximation differed by less than two percent from the fitted value at various pressures. As temperature is increased, the difference between the two values becomes negligible very quickly, and we conclude the steady state approximation is valid at temperatures above 450 K.

We note that while our master equation model reproduces experimental data very accurately, we can only speculate on how accurate the model is under conditions where experimental data is unavailable. For instance, the uncertainty in the computed high pressure rate coefficient k_∞ for the R → Int1p reaction could be significant, since none of our low temperature rate coefficient measurements appear to be anywhere near the high pressure limit. On the other hand, in the high temperature regime the master equation model correctly predicts the weak temperature dependence and the pressure independence of k_5 under conditions where experimental data is available. Therefore, there is no reason to suspect the model would not extrapolate well to high pressures and temperatures. We do not believe that other reaction channels become kinetically relevant even at 2000 K, because these reaction channels seem to involve barriers that are tens of kJ mol^{-1} higher in energy than TS1a and TS2a (see Fig. S1).

The self-reaction of 3-methylpropargyl has not been, to our knowledge, investigated, but the self-reaction of propargyl radical has been measured by several groups.[26–30] At combustion relevant conditions (500 − 2000 K), the pressure dependent bimolecular rate coefficient for the self-reaction of propargyl radical is between $3 \times 10^{-12} - 3 \times 10^{-11}$ cm^3 s^{-1}, while the nearly pressure independent $CH_3CCCH_2^{\bullet} + O_2$ rate coefficient is between $1 \times 10^{-14} - 5 \times 10^{-14}$ cm^3 s^{-1} (see Fig. 2). Assuming that the self-reaction of 3-methylpropargyl behaves similarly to the propargyl radical, the self-reaction at the high pressure limit would be roughly 2000 faster at 500 K and 400 times faster at 2000 K. To prevent the self-reaction from competing with the oxygen reaction at combustion temperatures, the oxygen concentration should be at least five orders of magnitudes larger than the radical concentration.

To facilitate utilization of the master equation results in combustion models, we provide modified Arrhenius representations in ChemKin PLOG format for the R → Int1p, R → Int1a, R → P, Int1p → R, Int1a → R, and Int1a → P rate coefficients in the Supplemental Material (PLOG.txt). The temperature and pressure ranges covered by the modified Arrhenius representations are 500 − 2000 K and 0.0001 − 100 atm.

MESMER was also used to calculate the following thermodynamic quantities for the R → Int1p reaction: standard enthalpy of reaction at 298 K ($\Delta_r H^{\ominus}_{298\ \mathrm{K}}$), standard entropy of reaction at 298 K ($\Delta_r S^{\ominus}_{298\ \mathrm{K}}$), and the correction function

$$f(T) = \frac{\Delta_r H^{\ominus}_T - \Delta_r H^{\ominus}_{298\ \mathrm{K}}}{RT} - \frac{\Delta_r S^{\ominus}_T - \Delta_r S^{\ominus}_{298\ \mathrm{K}}}{R} . \quad (9)$$

In a modified van't Hoff plot, the equilibrium constant measurements are corrected with the correction function $f(T)$ given by Eq. (9), which accounts for the small temperature dependence in $\Delta_r H^{\ominus}$ and $\Delta_r S^{\ominus}$.[9] A linear fit was made to the data with the intercept fixed with the computed $\Delta_r S^{\ominus}_{298\ \mathrm{K}}$ (third-law method). The slope of the linear fit gives the value for $\Delta_r H^{\ominus}_{298\ \mathrm{K}}$. For comparison purposes, we also provide the computed $\Delta_r H^{\ominus}_{298\ \mathrm{K}}$. We

obtained the following results:

$$\Delta_r S^{\ominus}_{298\ \mathrm{K}} = -136.6\ \mathrm{J\ mol^{-1}\ K^{-1}}\ \text{(computational)}$$
$$\Delta_r H^{\ominus}_{298\ \mathrm{K}} = -81.71 \pm 0.09\ \mathrm{kJ\ mol^{-1}}\ \text{(third-law)}$$
$$\Delta_r H^{\ominus}_{298\ \mathrm{K}} = -82.31\ \mathrm{kJ\ mol^{-1}}\ \text{(computational)}\ .$$

The uncertainty in $\Delta_r H^{\ominus}_{298\ \mathrm{K}}$ is the standard error (1σ) of the fit. As can be seen, the third-law result and the computational result differ only by 0.5 kJ mol^{-1}. We also computed the equilibrium constant for the R $\rightleftharpoons$ Int1p reaction with MESMER and compared it with the experimental values (see Fig. S4). The agreement is excellent.

6. Conclusions

We have investigated the kinetics and thermochemistry 3-methylpropargyl (but-2-yn-1-yl) reaction with molecular oxygen both experimentally and theoretically. Our experiments show that at low temperatures (223 − 304 K) the reaction proceeds by a barrierless addition, and the $CH_3CCCH_2^{\bullet}$ + O_2 reaction rate coefficient possesses negative temperature dependence and depends on bath gas density. At intermediate temperatures (340 − 395 K), the reaction equilibrates, and the equilibrium constant at different temperatures was determined from the time-dependent kinetic traces. At high temperatures (465 − 681 K), the bimolecular reaction rate coefficient shows positive temperature dependency and is independent of bath gas density. A bimolecular reaction product, ketene (ethenone), was observed at intermediate and high temperatures.

The structure and energetics of the relevant stationary points of the potential energy surface of the $CH_3CCCH_2^{\bullet}$ + O_2 reaction were calculated with DFT and high-level ab initio methods. The computed data was used in a master equation model of the reaction system. With small empirical adjustments of two rate-determining transition states, the model reproduced the experimental results accurately. The experimentally constrained model was extended to conditions relevant to combustion.

7. Acknowledgments

T. T. P. acknowledges support from the Doctoral Programme in Chemistry and Molecular Sciences of the University of Helsinki. A. J. E. acknowledges support from the Academy of Finland, Grant No. 288377. G. L. has been supported by the National Research, Development and Innovation Fund of Hungary, Grant K108966. The authors would also like to acknowledge COST Action CM1401 as well as CSC for access to computing resources.

References

[1] J. Zádor, C. A. Taatjes, R. X. Fernandes, Prog. Energy Combust. Sci. 37 (2011) 371 – 421.
[2] J. A. Miller, M. J. Pilling, J. Troe, Proc. Combust. Inst. 30 (2005) 43 – 88.
[3] N. Hansen, J. A. Miller, S. J. Klippenstein, P. R. Westmoreland, K. Kohse-Höinghaus, Combust. Explos. Shock Waves 48 (2012) 508–515.
[4] I. R. Slagle, D. Gutman, Proc. Combust. Inst. 21 (1988) 875 – 883.
[5] D. B. Atkinson, J. W. Hudgens, J. Phys. Chem. A 103 (1999) 4242–4252.
[6] D. K. Hahn, S. J. Klippenstein, J. A. Miller, Faraday Discuss. 119 (2002) 79–100.
[7] C. P. Moradi, A. M. Morrison, S. J. Klippenstein, C. F. Goldsmith, G. E. Douberly, J. Phys. Chem. A 117 (2013) 13626–13635.
[8] M. P. Rissanen, D. Amedro, A. J. Eskola, T. Kurten, R. S. Timonen, J. Phys. Chem. A 116 (2012) 3969–3978.
[9] V. D. Knyazev, I. R. Slagle, J. Phys. Chem. A 102 (1998) 1770–1778.
[10] Z. H. Lodhi, R. W. Walker, J. Chem. Soc., Faraday Trans. 87 (1991) 2361–2365.
[11] A. J. Eskola, R. S. Timonen, Phys. Chem. Chem. Phys. 5 (2003) 2557–2561.
[12] H. Yu, X. He, S. Louis Li, D. G Truhlar, Chem. Sci. 7 (2016) 50325051.
[13] F. Weigend, R. Ahlrichs, Phys. Chem. Chem. Phys. 7 (2005) 3297–3305.
[14] J. L. Bao, J. Zheng, I. M. Alecu, B. J. Lynch, Y. Zhao, D. G. Truhlar, 2017. available at `https://comp.chem.umn.edu/freqscale/version3b2.htm`.
[15] M. J. Frisch, et al., Gaussian16 Revision B.01, 2016. Gaussian Inc. Wallingford CT.
[16] J. D. Watts, J. Gauss, R. J. Bartlett, J. Chem. Phys. 98 (1993) 8718–8733.
[17] D. R. Glowacki, C.-H. Liang, C. Morley, M. J. Pilling, S. H. Robertson, J. Phys. Chem. A 116 (2012) 9545–9560.
[18] R. X. Fernandes, K. Luther, J. Troe, J. Phys. Chem. A 110 (2006) 4442–4449.
[19] T. J. Lee, P. R. Taylor, Int. J. Quantum Chem. 36 (1989) 199–207.
[20] Y. Zhao, D. G. Truhlar, Theor. Chem. Acc. 120 (2008) 215–241.
[21] C. F. Goldsmith, L. B. Harding, Y. Georgievskii, J. A. Miller, S. J. Klippenstein, J. Phys. Chem. A 119 (2015) 7766–7779.
[22] C. F. Goldsmith, A. S. Tomlin, S. J. Klippenstein, Proc. Combust. Inst. 34 (2013) 177 – 185.
[23] C. F. Goldsmith, W. H. Green, S. J. Klippenstein, J. Phys. Chem. A 116 (2012) 3325–3346.
[24] A. W. Jasper, J. A. Miller, J. Phys. Chem. A 113 (2009) 5612–5619.
[25] C. W. Gao, J. W. Allen, W. H. Green, R. H. West, Comput. Phys. Commun. 203 (2016) 212 – 225.
[26] E. V. Shafir, I. R. Slagle, V. D. Knyazev, J. Phys. Chem. A 107 (2003) 8893–8903.
[27] B. R. Giri, H. Hippler, M. Olzmann, A. N. Unterreiner, Phys. Chem. Chem. Phys. 5 (2003) 4641–4646.
[28] R. Fernandes, H. Hippler, M. Olzmann, Proc. Combust. Inst. 30 (2005) 1033 – 1038.

[29] S. Scherer, T. Just, P. Frank, Proc. Combust. Inst. 28 (2000) 1511 – 1518.
[30] Y. Georgievskii, J. A. Miller, S. J. Klippenstein, Phys. Chem. Chem. Phys. 9 (2007) 4259–4268.

8. Separate List of Captions

Fig. 1: **(a):** A typical bimolecular plot at low temperature. A radical decay signal in the absence of O_2 is shown in the bottom right corner. A radical decay signal with added oxygen is shown in the top left corner. **(b):** A modified van't Hoff plot of $\ln(K) + f(T)$ versus reciprocal temperature. See text for details.**(c):** A typical bimolecular plot at high temperature. A radical decay signal with added oxygen is shown in the bottom right corner. The corresponding formation signal for ketene is shown in the top left corner. The radical decay rate is 49.6 ± 1.5 s^{-1} and the ketene formation rate is 50.3 ± 4.1 s^{-1}. The uncertainties are the standard errors (1σ) of the fits.

Fig. 2: The symbols in the left and right subfigures depict the $CH_3CCCH_2^{\bullet}$ + O_2 bimolecular rate coefficient measured at different temperatures and pressures. The experimental results (symbols) are shown alongside the results produced by our master equation model (lines).

Fig. 3: A reaction enthalpy profile at zero kelvin corresponding to the part of the PES of reaction $CH_3CCCH_2^{\bullet}$ + O_2 that is included in our master equation model. Elementary steps that do not significantly affect the overall kinetics of $CH_3CCCH_2^{\bullet}$ + O_2 have been omitted.

Table 1: Energies of the stationary points on the $CH_3CCCH_2^{\bullet}$ + O_2 PES that are included in our master equation model. All energies are relative to the reactant energy. The table lists the T1 diagnostic, the electronic energy at the complete basis set limit (see Equation (6)), the zero-point energy and the zero-point corrected electronic energy (standard enthalpy of reaction at zero kelvin). The final column shows the experimentally adjusted $\Delta_r H_0^{\ominus}$ used in our master equation model.

9. List of Supplemental Material

The supplemental material consists of four files, supplementalFiguresAndTables.pdf, geometries.txt, PLOG.txt, and mesmerInputFile.xml.

10. Separate List of Captions for Supplemental Material

Fig. S1: A reaction enthalpy profile at zero kelvin for the potential energy surface of $CH_3CCCH_2^\bullet + O_2$ reaction. The enthalpies presented here were calculated at the MN15/Def2TZVP level of theory. See Table S1 and Fig. S2 for details about each stationary point. For species with *cis*/*gauche*/*trans* isomerism, only the lowest energy isomer is shown.

Fig. S2: The structures of the stationary points on the $CH_3CCCH_2^\bullet + O_2$ potential energy surface.

Fig. S3: **(a):** The temperature dependence of some of the unimolecular elementary reaction rate coefficients returned by our master equation mode at 0.0001 atm and 100 atm. **(b):** The temperature dependence of the bimolecular elementary reaction rate coefficients returned by our master equation mode at 0.0001 atm and 100 atm. See main text for details about the effective $R \rightarrow P$ channel. **Fig. S4**: A plot showing the agreement between the computed and measured equilibrium constant for the $CH_3CCCH_2^\bullet + O_2 \rightleftharpoons CH_3CCCH_2OO^\bullet$ (Int1p) reaction.

Table S1: Relative Energies of the Stationary Points on the $CH_3CCCH_2^\bullet + O_2$ Potential Energy Surface.

Table S2: The Experimental Conditions and Results for the $CH_3CCCH_2^\bullet + O_2$ Bimolecular Rate Coefficient Measurements.

Table S3: The Experimental Conditions and Results for the $CH_3CCCH_2^\bullet + O_2 \underset{\beta}{\overset{\alpha}{\rightleftharpoons}} CH_3CCCH_2OO^\bullet$ (Int1p) Equilibrium Constant Measurements.

Table S4: Values of the Fit Parameters for the Double Exponential Fitting Function $[R^\bullet](t) = A + Be^{-\lambda_1 t} + Ce^{-\lambda_2 t}$.